AIAA AVIATION Forum
August 2-6, 2021, VIRTUAL EVENT
AIAA AVIATION 2021 FORUM

10.2514/6.2021-2817

Navigation in odor plumes: How do the flapping kinematics modulate the odor landscape?

Menglong Lei[1*], John P. Crimaldi[2†], Chengyu Li[1‡]

[1]*Villanova University, Villanova, PA 19085;* [2]*University of Colorado, Boulder, CO 80303*

Insects rely on their olfactory system to forage, prey, and mate. They can sense odor emitted from sources of their interest, use their highly efficient flapping-wing mechanism to follow odor trails, and track down odor sources. During such an odor-guided navigation, flapping wings not only serve as propulsors for generating lift and maneuvering, but also actively draw odors to the antennae via wing-induced flow. This helps enhance olfactory detection by mimicking "sniffing" in mammals. However, due to a lack of quantitative measuring tools and empirical evidence, we have a poor understanding of how the induced flow generated by flapping kinematics affects the odor landscape. In the current study, we designed a canonical simulation to investigate the impact of flapping motion on the odor plume structures. A sphere was placed in the upstream and releases odor at the Schmidt number of 0.71 and Reynolds number of 200. In the downstream, an ellipsoidal airfoil underwent a pitch-plunge motion. Both two- and three-dimensional cases are simulated with Strouhal number of 0.9. An in-house immersed-boundary-method-based CFD solver was applied to investigate the effects of flapping locomotion on the wake topology and odor distribution. From our simulation results, remarkable resemblances were observed between the wake topology and odor landscape. For the 2D case, an inverse von Kármán vortex street was formed in the downstream. For the 3D case, the wake bifurcates and forms two branches of horseshoe-like vortices. The results revealed in this study have the potential to advance our understanding of the odor-tracking capability of insects navigation and lead to transformative advancements in unmanned aerial devices that will have the potential to greatly impact national security equipment and industrial applications for chemical disaster, drug trafficking detection, and GPS-denied indoor environment.

Nomenclature

C	= Odor concentration	T	= Normalized temperature
C^*	= Normalized odor concentration	u_i	= Velocity component
P	= Pressure	U_i	= Face-centered velocity component
Pr	= Prandtl number	t	= Time
Re	= Reynolds number	α	= Energy/Odor diffusivity
Sc	= Schmidt number	ν	= Kinematic diffusivity
St	= Strouhal number	ρ	= Density

* PhD Candidate, Department of Mechanical Engineering, AIAA Student Member

† Professor, Department of Civil, Environmental and Architectural Engineering

‡ Assistant Professor, Department of Mechanical Engineering, AIAA Member, chengyu.li@villanova.edu

I. Introduction

AIRBORNE odor plumes exhibit complex spatiotemporal structure in a natural environment characterized by unsteady and intermittent concentration fields. The distribution of odor plume structure can be visualized as an "odor landscape" consisting of evolving valleys and peaks, in which the elevation represents the strength of a particular odorant concentration [1]. At low Reynolds number and low Péclet number, the odor spreads primarily by diffusion, and the odor landscape presents smooth odorant concentration. In a turbulent regime, however, the odor plume structures are shaped into intermittent whiffs separated by stochastic durations of background air (blanks). Wright [2] first successfully applied a Gaussian plume model to estimate the time-averaged concentration of insect pheromones downwind of a source. As one might expect, the average concentration decreases with the downwind distance from the source, and the average concentration on the midline of the plume decays with a power law. However, subsequent studies [3, 4] indicated that insects do not respond to the mean concentration as predicted by the Gaussian distribution model. Instead, insects respond to instantaneous concentrations that are frequently many-fold higher than the mean concentrations. To investigate the instantaneous odorant concentration, experimental studies [5-8] measured the plume dispersing, and indicated that the fluctuations of concentration decrease with downwind distance, steeper close to the source, and more gradually at large distances. At a given downwind distance, the fluctuations of concentration increased in crosswind direction with a distance from the plume centerline. The probability density function model could provide an adequate description of the fluctuation statistics of the odor landscapes. In addition to the fluctuations, the discontinuous nature of whiffs and blanks causes the concentration intermittency. Celani et al.[9] used a Lagrangian approach to solve the advection-diffusion equations and demonstrated that the intermittency is a function of downwind distance from the source. Their results illustrated that the distributions of whiff durations and blank durations follow a power law with an exponent of -3/2.

Despite considerable experimental and theoretical studies on the spatiotemporal structures of odor landscapes, however, no attempts have been made to incorporate the effects of wing-induced flow into the predictive model for the concentration fluctuations and intermittency. A number of experimental studies [10, 11] and numerical studies [12-15] have indicated that the local odor concentration can be enhanced significantly by the induced flow generated by flapping wings [16]. One might expect the unsteady flow generated by flapping wings would perturb the odor plume structure and odorant transport around the olfactory receptors of insects (i.e., antennae), and thus impact how the insects perceive the global odor landscape. To date, it still remains unclear how wing-induced flow affects the spatiotemporal structure of the odor landscape in odor-guided aeronautic navigation of insects.

The purpose of the present study is to evaluate the odor trapping process in a canonical pitching-plunging setup. A series of numerical simulations are performed using an in-house immersed-boundary-method-based CFD solver. Detailed analyses of aerodynamic performance and its associated odor concentration are presented and compared for two- and three-dimensions.

II. Methodology

A. Numerical methods

The numerical simulation employed in the current study is based on an in-house immersed-boundary-method Navier-Stokes equations solver. The 3-D viscous incompressible Navier-Stokes equations are written as follows:

$$\begin{cases} \dfrac{\partial u_i}{\partial x_i} = 0 \\ \dfrac{\partial u_i}{\partial t} + \dfrac{\partial \left(u_i u_j\right)}{\partial x_j} = -\dfrac{1}{\rho}\dfrac{\partial P}{\partial x_i} + \nu \dfrac{\partial}{\partial x_j}\left(\dfrac{\partial u_i}{\partial x_j}\right) \end{cases} \tag{1}$$

Where u_i are the velocity components, P is the pressure, ρ is the fluid density, ν is the kinematic viscosity.

The above equations are discretized using a cell-centered, collocated arrangement of the primitive variables and are solved using the finite difference-based Cartesian grid immersed boundary method. To facilitate the discretization, the face-centered velocities, U_i, are computed by interpolation of the adjacent cell-centered velocities u_i. The equations are integrated with time using the fractional step method. In the first sub-step, a modified momentum equation is discretized using the implicit Crank-Nicolson scheme. The intermediate cell-centered velocities u_i^* are obtained by solving the following equation in the first sub-step.

$$\frac{u_i^* - u_i^n}{\Delta t} + \frac{1}{2}\left(3\frac{\delta U_j^n u_i^n}{\delta x_j} - \frac{\delta U_j^{n-1} u_i^{n-1}}{\delta x_j}\right) = -\frac{1}{\rho}\frac{\delta P^n}{\delta x_i} + \frac{\nu}{2}\left[\frac{\delta}{\delta x_i}\left(\frac{\delta u_i^*}{\delta x_i}\right) + \frac{\delta}{\delta x_i}\left(\frac{\delta u_i^n}{\delta x_i}\right)\right] \tag{2}$$

In the second sub-step, the following pressure Poison equation is solved to obtain the pressure correction P'.

$$\frac{1}{\rho}\frac{\delta}{\delta x_i}\left(\frac{\delta P'}{\delta x_i}\right) = \frac{1}{\Delta t}\frac{\delta U_i^*}{\delta x_i} \tag{3}$$

Where U_i^* are the face-centered intermediate velocities interpolated by the cell-centered velocities u_i^*. The velocity and pressure field are updated from the previously obtained intermediate velocities u_i^* and the pressure correction P' as

$$\begin{aligned} P^{n+1} &= P^n + P' \\ u_i^{n+1} &= u_i^* - \Delta t \frac{1}{\rho}\frac{\delta P'}{\delta x_i} \end{aligned} \tag{4}$$

With the velocity field U_i, the odor transportation equation is then solved to obtain the instantaneous odor concentration. The governing equation of odorant convection and diffusion is given below.

$$\frac{\partial C}{\partial t} + \frac{\partial C U_i}{\partial x_i} = \alpha \frac{\partial^2 C}{\partial x_i^2} \tag{5}$$

Where C is the odor concentration, α is the odor diffusivity. The equation is discretized using an implicit Crank-Nicolson scheme

$$\frac{C^{n+1} - C^n}{\Delta t} + \frac{\delta C^n U_i^n}{\delta x_i} = \frac{\alpha}{2}\left[\frac{\delta}{\delta x_i}\left(\frac{\delta C^{n+1}}{\delta x_i}\right) + \frac{\delta}{\delta x_i}\left(\frac{\delta C^n}{\delta x_i}\right)\right] \tag{6}$$

Schmidt number Sc, the ratio between kinematic viscosity and odor diffusivity ($\mathrm{Sc} = \nu / \alpha$), is used to indicate the odor diffusion intensity. When Sc is small, odor diffusion dominant the odor transportation. While large Sc indicates odor convection dominant the odor transportation.

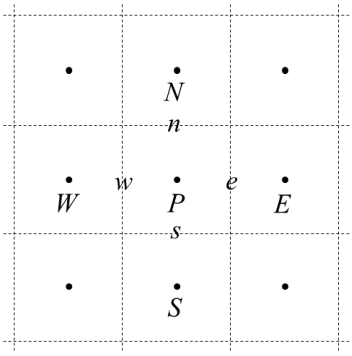

Figure 1. Schematic of the grid. The uppercase letters denote cell-centered variables, the lowercase letters denote the face-centered variables.

The advantage of immersed boundary method is that the flow field can be simulated without the need of generating body conformal grids. This eliminates the need for complicated re-meshing algorithms for moving boundaries. The Eulerian form of the Navier-Stokes equations is discretized on a Cartesian mesh and the boundary conditions on the immersed boundary are imposed through a "ghost-cell" procedure. The pressure Poisson equation is solved using the semi-coarsening multi-grid method with immersed-boundary methodology. The current numerical treatment can eliminate the need for mesh regeneration at each time step, and thus save the computation cost. This in-house flow solver has been successfully applied to study canonical revolving wings[17-19], flapping propulsion problems[20-24], and insect flight[14, 25-27]. Details and validations of this solver on the velocity field can be found in the author's previous papers [22, 25].

The current paper mainly focuses on the discretization and calculation of the odor concentration. The odor advection-diffusion equation is discretized on a 3-D Cartesian grid, as shown in Figure 1. The finite differential equation is written as

$$\begin{aligned} C_P^{n+1} - \frac{\alpha\Delta t}{2}\left(a_W C_W^{n+1} + a_E C_E^{n+1} + a_N C_N^{n+1} + a_S C_S^{n+1} + a_B C_B^{n+1} + a_F C_F^{n+1} + a_P C_P^{n+1}\right) = \\ C_P^n - \Delta t\left(\frac{C_e^n U_e^n - C_w^n U_w^n}{\Delta x} + \frac{C_n^n U_n^n - C_s^n U_s^n}{\Delta y} + \frac{C_f^n U_f^n - C_b^n U_b^n}{\Delta z}\right) \\ + \frac{\alpha\Delta t}{2}\left(a_W C_W^n + a_E C_E^n + a_N C_N^n + a_S C_S^n + a_B C_B^n + a_F C_F^n + a_P C_P^n\right) \end{aligned} \tag{7}$$

Where variables with lowercase subscript are the face-centered variables calculated by interpolation of the adjacent cell-centered variables. The coefficients a_W, a_E, a_N, a_S, a_B, a_F, a_P are calculated by discretizing the diffusion term.

$$\begin{aligned} \frac{\delta}{\delta x_i}\left(\frac{\delta C}{\delta x_i}\right) &= \frac{\frac{C_E - C_P}{\Delta x} - \frac{C_P - C_W}{\Delta x}}{\Delta x} + \frac{\frac{C_N - C_P}{\Delta y} - \frac{C_P - C_S}{\Delta y}}{\Delta y} + \frac{\frac{C_F - C_P}{\Delta z} - \frac{C_P - C_B}{\Delta z}}{\Delta z} \\ &= a_E C_E + a_W C_W + a_N C_N + a_S C_S + a_F C_F + a_B C_B + a_P C_P \end{aligned} \tag{8}$$

B. Solver validation

The form of the odor advection-diffusion equation is identical to the form of the energy equation. To validate the numerical solver for odor transportation, we compared our calculation results of 2-D flow past a rotating cylinder with the results by Yan and Zu using the Lattice Boltzmann Method [28], and the results of 3-D calculation of flow past a stationary cube and sphere with the results of Richter and Nikrityuk using a commercial CFD solver [29], as shown in Figure 2.

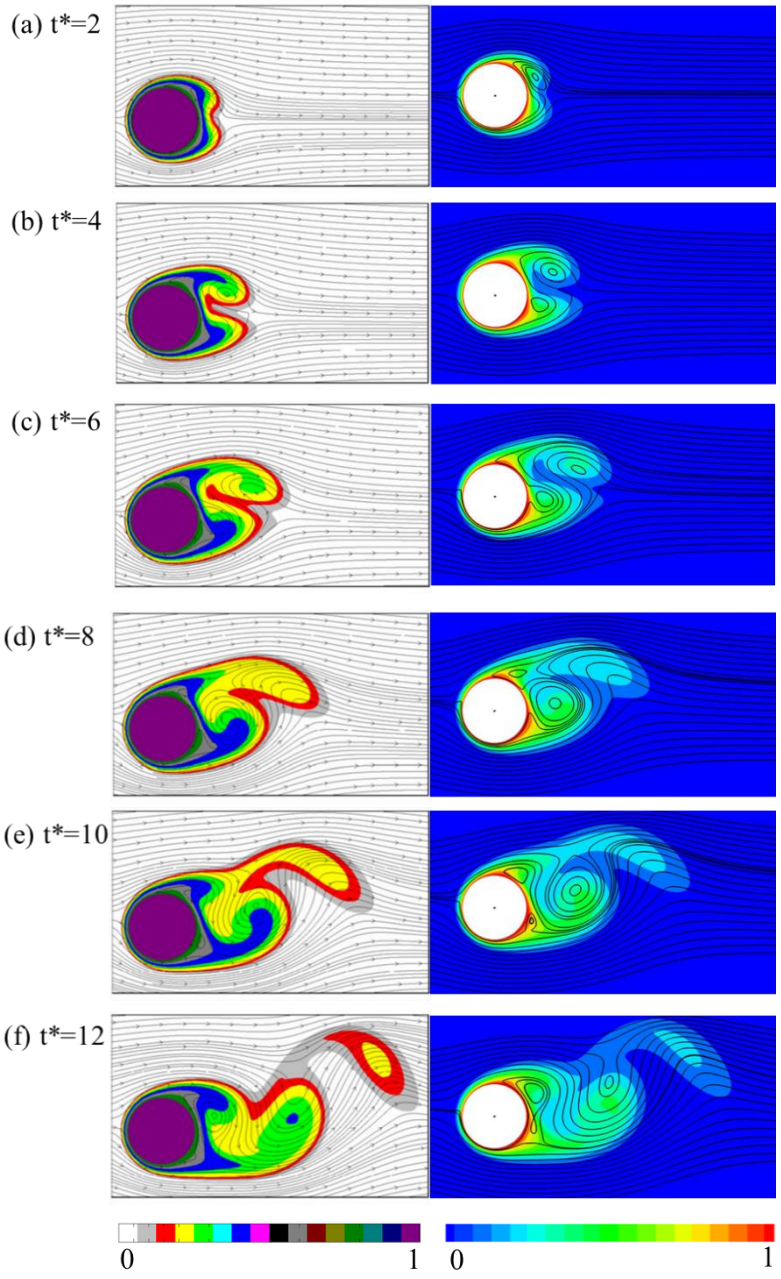

Figure 2. Comparison of evolution of the streamline and temperature field for Re = 200, k = 0.5, Pr = 0.5 (left: computation by Yan and Zu [28]; right: current study).

In the 2-D flow past a rotating cylinder case, viscous incompressible fluid flow past a counterclockwise rotating isothermal cylinder is simulated using the lattice Boltzmann method. The Reynolds number is defined as $\mathrm{Re} = UD/\nu$, and parameter $k = V/U$, in which U is the inflow velocity, V is the rotational velocity of the cylinder, and D is the diameter of the cylinder. As shown in Figure 2, the temperature contour and streamline in our simulation results agree well with the literature [28].

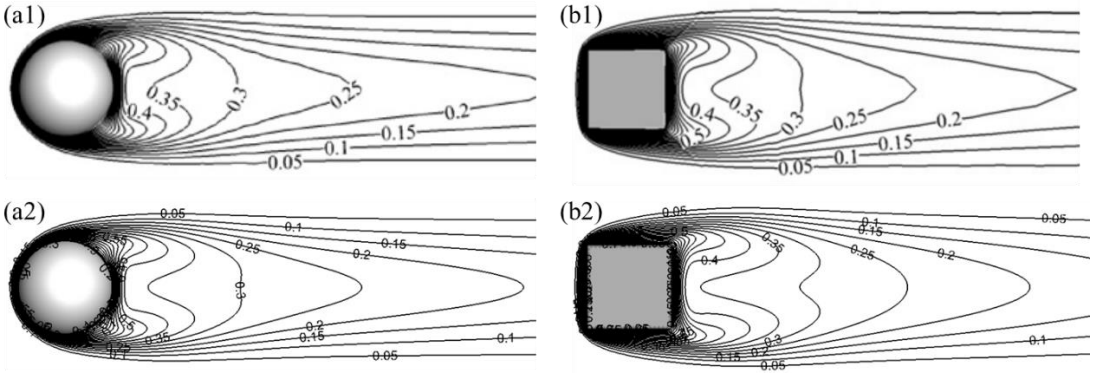

Figure 3. Comparison of temperature contour for Re = 200, Pr = 0.744. (a1) and (b1) are results calculated by Richter and Nikrityuk [29]. (a2) and (b2) are results from current paper.

For the 3-D flow past a stationary sphere and cube case, the comparison of the temperature contour on the symmetry plane is presented in Figure 3. Our CFD results are also consistent with the data reported by Richter and Nikrityuk [29].

C. Simulation setup

The current study simulated a fixed sphere and a thin ellipsoidal airfoil that undergoes a pitch-plunge motion both two- and three-dimensionally. The simulations are performed in a 672×416 non-uniform 2-D and a 352×224×160 non-uniform 3-D Cartesian grid. Both the 2-D and 3-D simulations employ the same prescribed kinematics, as shown in Figure 4. The cylinder and ellipse airfoil used in the 2-D case are replaced by 3-dimensional sphere and ellipsoidal airfoil in the 3-D case to study the effects of spanwise flow on the vortex structures and its associated odor plume structures. The stationary sphere fixed in the upstream is releasing odor at concentration C_h. The airfoil has zero-gradient odor boundary condition and undergoes a pitch-plunge motion combined by the translation in the *y*-axis according to Eq. (9) and the rotation about its center along the *z*-axis according to Eq. (10).

$$y(t) = \frac{L}{2}\sin(2\pi f t^*) \tag{9}$$

$$\theta(t) = -\frac{\pi}{6}\cos(2\pi f t^*) \tag{10}$$

Where t^* is the non-dimensional time defined as $t^* = Ut/L$.

The sphere and airfoil employed in the 3-D simulation are shown in Figure 5. In which the diameter of the sphere is *D*, the scale of the ellipsoidal airfoil in the three directions is denoted as a_x, a_y, and a_z. The Reynolds number in the current study is 200, which is defined as $\mathrm{Re} = UL/\nu$, where L is the reference

length, $L = D = a_x$, $a_y = 0.24a_x = 0.12a_z$, f is the flapping frequency. The distance between the sphere center and the airfoil center is $3L$. The Schmidt number Sc = 0.71 is defined as $\mathrm{Sc} = \nu / \alpha$, where α is the odor diffusivity. The Strouhal number St is used to characterize the pitch-plunge motion, defined as $\mathrm{St} = Lf / U$. In the following simulations, St = 0.9.

The sphere and ellipsoidal airfoil are surrounded by a cuboid region with high grid resolution. Around the dense region, there is a secondary dense region with a lower grid resolution. At the inlet boundary, the Dirichlet boundary condition was applied with constant incoming flow velocity and odor concentration. At the downstream boundary, the Neumann boundary condition was provided. The zero-gradient boundary condition was applied at all lateral boundaries. A homogeneous Neumann boundary condition was used for pressure at all these boundaries. Nonslip boundary conditions were applied on the surfaces of the sphere and airfoil.

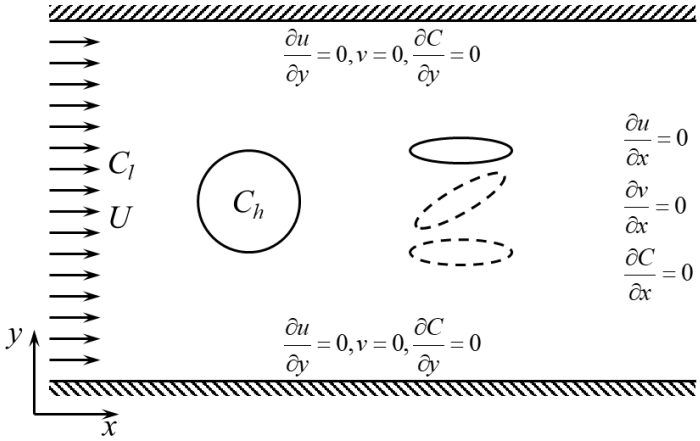

Figure 4. Flow field setup. The velocity and odor concentration at the flow inlet are U and C_l. The sphere is fixed in the upstream and the odor concentration is C_h. The ellipsoidal airfoil undergoes a pitch-plunge motion and has a zero-gradient odor boundary condition.

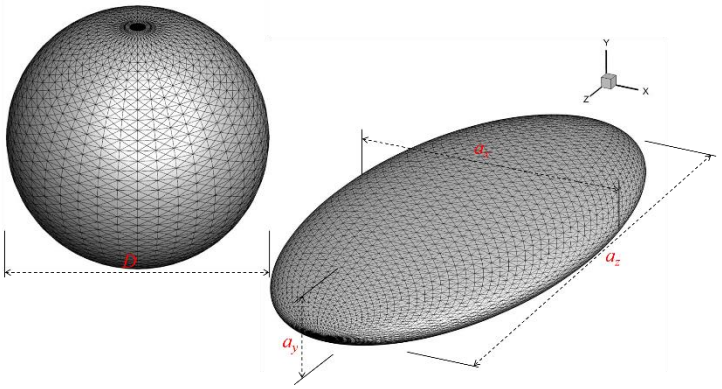

Figure 5. The sphere odor source and ellipsoidal airfoil used in the current study. The surfaces of the sphere and ellipsoidal airfoil are represented by an unstructured grid consisting of triangular elements.

To visualize the odor concentration field and vorticity field, two non-dimensional parameters are used in the following discussion, the non-dimensional odor concentration defined in Eq. (11) and the non-dimensional spanwise vorticity defined in Eq. (12).

$$C^* = \frac{C - C_l}{C_h - C_l} \tag{11}$$

$$\omega_z^* = \frac{\omega_z L}{U} \tag{12}$$

III. Results and Discussion

In section A, we present the 2-D simulation results of odor concentration distribution and wake topology. Section B shows the results of the 3-D simulation. A comprehensive description of the evolution of wake topology and odor concentration is presented and compared side by side. To make sure the flow and odor field reach a periodic state, all the data and pictures are chosen from the 10th pitch cycle.

A. Wake topology and odor plume concentration for the two-dimensional simulation

To visualize how the pitch-plunge motion disturbs the odor field, the cycle-averaged odor concentration contour is shown in Figure 6(a). The blue ellipses denote the position of the pitch-plunge airfoil. A cylinder in the upstream is releasing odor at $C^* = 1$. The pitch-plunge airfoil draws the odor plume from the odor source and significantly disturbs the odor field in the downstream. Figure 6(b) shows the probability density function (PDF) of the odor concentration in the flow field, which is the percentage of the area of different odor concentration levels. The PDF is maximized near $C^* = 0$. A trough is observed near $C^* = 0.2$. The possible reason is that the odor concentration decreases significantly because of the pitch-plunge motion of the airfoil.

Figure 7 shows the instantaneous wake structure visualized by vorticity and odor concentration contour at mid-upstroke (t/T = 0), end-of-upstroke (t/T = 0.25), mid-downstroke (t/T = 0.5), and end-of-downstroke (t/T = 0.75), respectively. The pitch-plunge motion of the airfoil creates two sets of vortices that advect downstream. The rotation direction of the vortices is related to when and where the vortices are generated. The vortices that rotate clockwise are represented by blue contour and are generated from the upper surface of the airfoil during the upstroke. The vortices that rotate counterclockwise are represented by red contour and are generated from the lower surface during the downstroke. Figure 7(a2), (b2), (c2), (d2) show the evolution of odor concentration. Surprisingly, the contours of vorticity and odor plume structure are remarkably similar in shape.

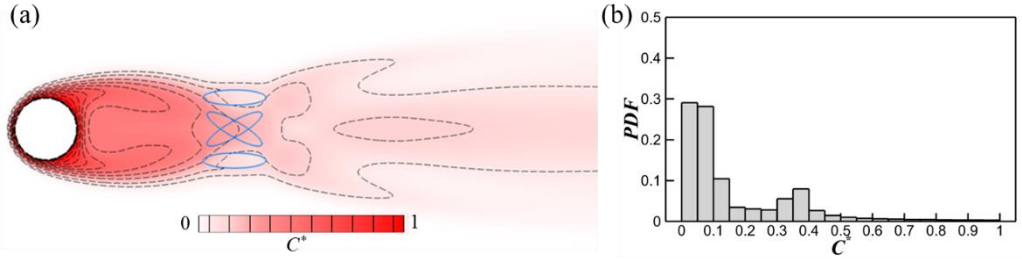

Figure 6. Cycle-averaged odor concentration contour (a) and probability density functions (PDF) of odor concentration in the flow field (b) for the two-dimensional simulation.

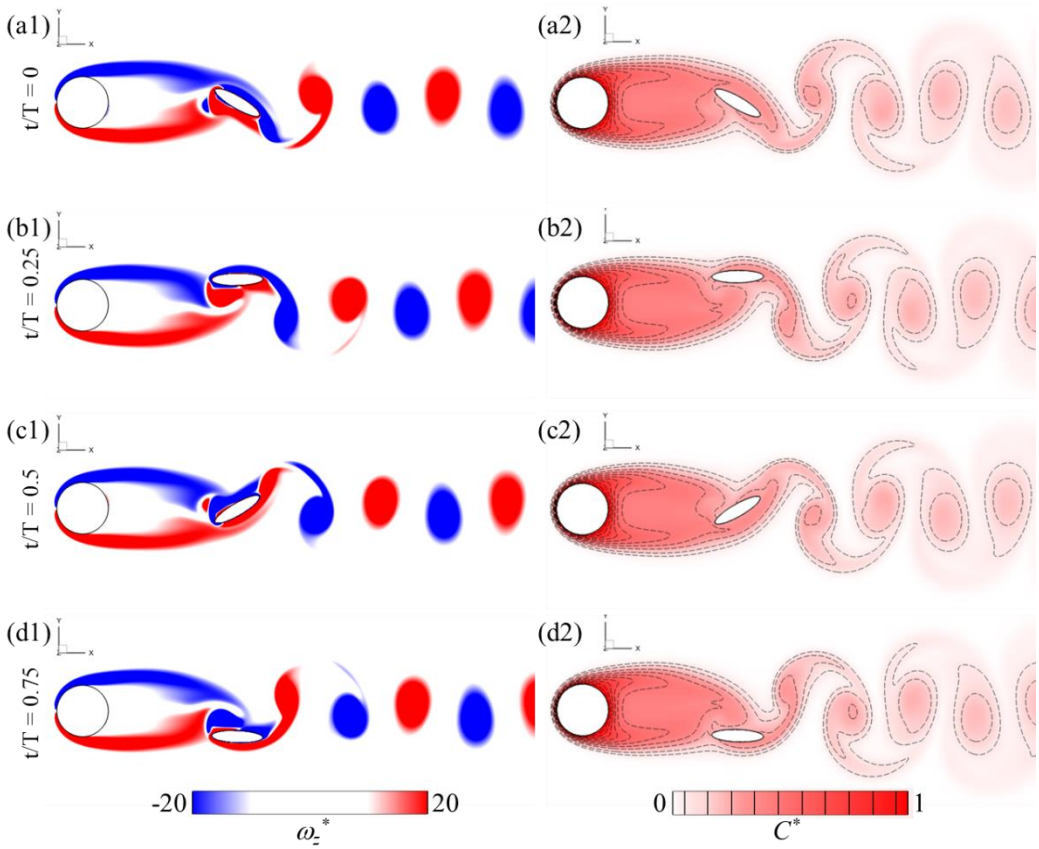

Figure 7. The wake structure visualized by vorticity ω_z^* at t/T = 0 (a1), 0.25 (b1), 0.5 (c1), and 0.75 (d1), and odor concentration contour at t/T = 0 (a2), 0.25 (b2), 0.5 (c2), and 0.75 (d2) for the two-dimensional simulation.

B. Wake topology and odor plume concentration for the three-dimensional simulation

Figure 8(a), (b), and (c) show the perspective, side, and top views of the wake topology using the Q criterion at mid-upstroke. The pitch-plunge motion of the airfoil creates two sets of vortex rings that advect downstream upward and downward, forming a bifurcation angle of 37°. The advection direction of the vortex rings is related to the process by which the vortex rings are formed and shed. The vortex rings that advect upward are formed and released on the upper surface of the airfoil trailing edge. And the set of vortex rings that moves downward are released from the lower surface of the airfoil trailing edge. In Figure 8(a), (b), and (c), a vortex ring V_1 that moves upward and a vortex ring V_2 that moves downward are identified by arrow lines whose direction indicates the rotation direction of the vortex ring. The vortex ring V_2 is formed in the present half-stroke and connecting to the trailing edge vortex. The vortex ring V_1 is formed at the previous half-cycle and moves at an oblique angle on the symmetry plane. Figure 8(d) is the contour plot of spanwise vorticity on the symmetry plane. It appears that the wake topology (Figure 8(b)) is not consistent with the vorticity contour (Figure 8(d)). The reason is the vortex rings are distributed three-dimensionally in space, while the vorticity contour only shows the vorticity on the symmetry plane.

Figure 9(a) shows the cycle-averaged odor concentration contour on the symmetry plane. The ellipsoidal airfoils denote the position of the pitch-plunge motion. Similar to the 2-D simulation, a sphere is releasing

odor at $C^* = 1$, with a pitch-plunge airfoil flapping downstream. Figure 9(b) shows the probability density function of the odor concentration on the symmetry plane. Differences in odor plume structure after the airfoil are observed between the 2-D and 3-D simulations. The odor plume distributes wider in the *y*-direction and dissipates quicker as it advects downstream.

Figure 10 shows the wake topology, normalized odor iso-surface at $C^* = 0.05$, and odor contour on the symmetry plane during a pitch cycle. The vortices in Figure 10 are 3-D vortex rings that formed by tip vortices released from the airfoil tip. It is interesting to notice that the shapes of vortex structures and odor iso-surface are similar for the 3-D simulation too. The odor concentration is higher where the two tip vortices join together and lower where the two tip vortices separate. The odor plume and vortices dissipate quickly as they advect downstream. The possible reason is that as odor plumes travel with the fluid, they also dissipate into the ambient fluid. Another difference between the vortex topology and odor plume structure is while the two sets of vortex rings do not join each other and separate as they advect downstream upward and downward, the downstream odor field remains continuous, as shown in the odor contour in Figure 10.

In conjunction with the 2-D and 3-D simulations, we noticed significant differences in wake topology and odor plume structure, even with the same setup. For the 2-D case, the vortices advect downstream horizontally and remain intact for a long distance (Figure 7). For the 3-D case, two sets of vortices bifurcate and advect upward and downward respectively at an oblique angle and dissipate quicker to the ambient fluid (Figure 10). For both cases, the wake topology and odor plume structure are similar in shape.

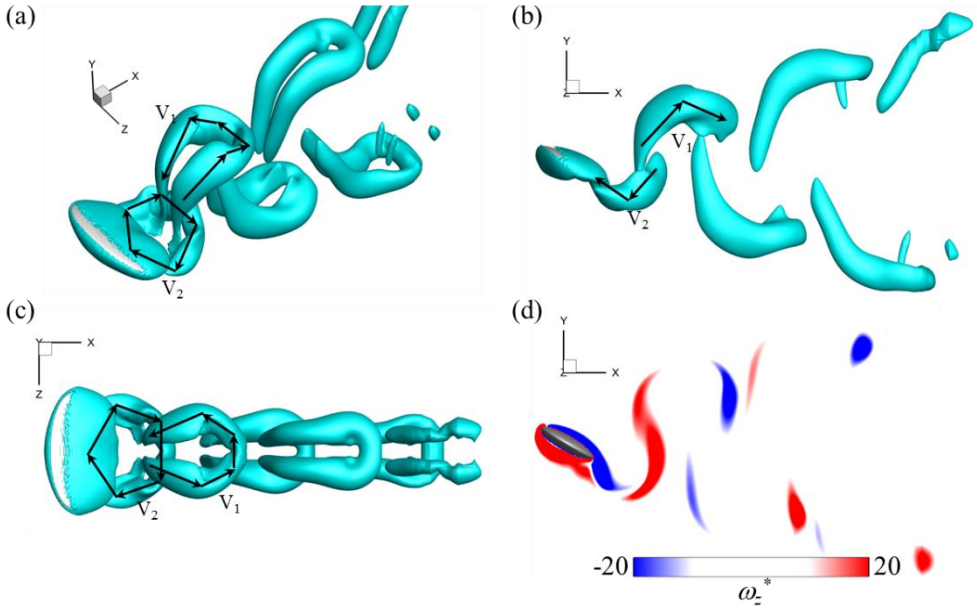

Figure 8. Perspective view (a), side view (b), and top view (c) of wake topology visualized by Q criterion. And spanwise vorticity contour plot on the symmetry plane (d) at mid-upstroke.

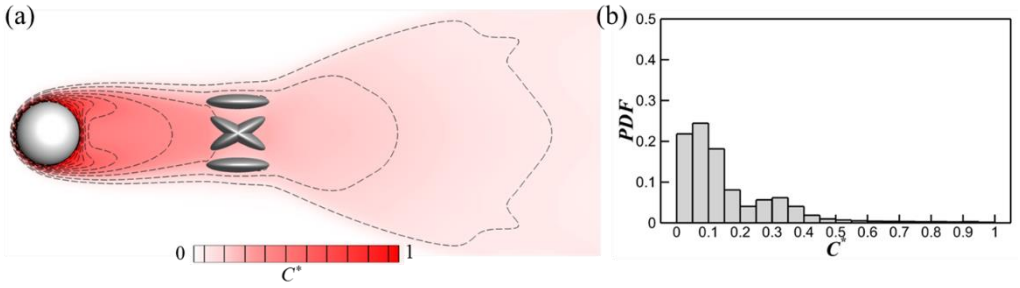

Figure 9. Cycle-averaged odor concentration contour (a) and probability density functions (PDF) of odor concentration in the flow field (b) for the three-dimensional simulation.

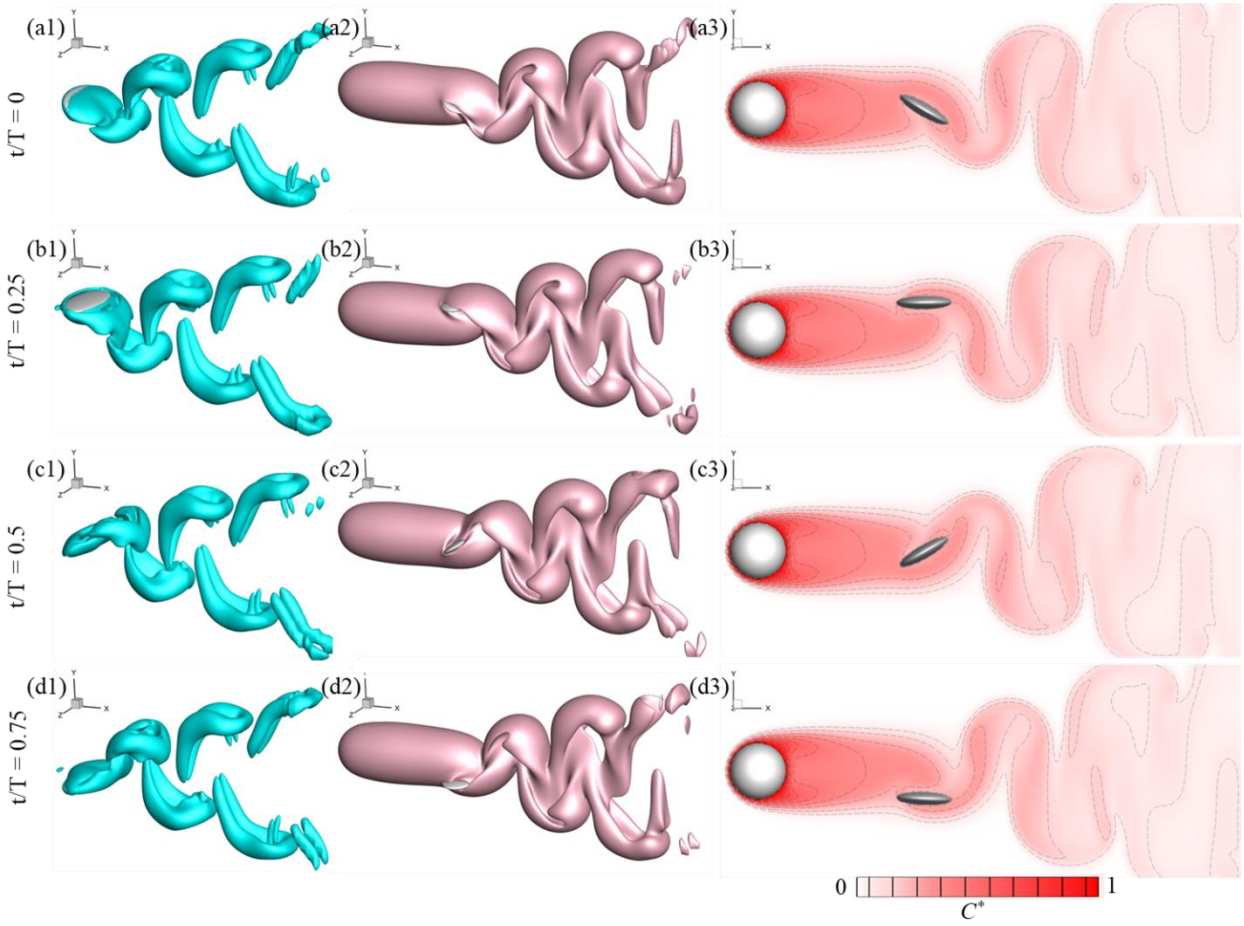

Figure 10. Perspective view of wake topology visualized by Q criterion at $t^* = 0$ (a1), 0.25 (b1), 0.5 (c1), and 0.75 (d1). Perspective view of iso-surface of normalized odor concentration $C^* = 0.05$ at $t^* = 0$ (a2), 0.25 (b2), 0.5 (c2), and 0.75 (d2). Normalized odor concentration contour on the symmetry plane at $t^* = 0$ (a3), 0.25 (b3), 0.5 (c3), and 0.75 (d3).

IV. Conclusions

In this study, an immersed-boundary-method-based CFD solver was used to solve the 3D Navier-Stokes equations. Based on the calculation results of the velocity field, the odor advection-diffusion equation was then solved to obtain the odor concentration field at each time step. The calculation results for both the 2-D and 3-D simulations confirmed that the flow induced by pitch-plunge airfoil significantly impacts the odor plume structure. Remarkable resemblances between the shape of wake topology and odor plume structure were observed for all the cases. The 2-D and 3-D simulations employ the identical setup, but the wake topology and odor plume are quite different. For the 2D case, an inverse von Kármán vortex street was formed in the downstream. For the 3D case, the vortices bifurcate and form two branches of horseshoe-like vortices.

Acknowledgments

This research is supported by the National Science Foundation (CBET-2042368) and the 2019 ORAU Ralph E. Powe Junior Faculty Enhancement Award to C. Li and the National Science Foundation (DBI-2014217) to J. P. Crimaldi. All simulations were run on the High-Performance Computing Cluster of the College of Engineering at Villanova University.

References

1. Pannunzi, M., and Nowotny, T. "Odor stimuli: Not just chemical identity," *Frontiers in Physiology* Vol. 10, 2019.

2. Wright, R. "The olfactory guidance of flying insects," *The Canadian Entomologist* Vol. 90, No. 2, 1958, pp. 81-89.

3. Murlis, J., and Jones, C. "Fine‐scale structure of odour plumes in relation to insect orientation to distant pheromone and other attractant sources," *Physiological Entomology* Vol. 6, No. 1, 1981, pp. 71-86.

4. Elkinton, J. S., and Cardé, R. T. "Odor dispersion," *Chemical Ecology of Insects*. Springer, 1984, pp. 73-91.

5. Mylne, K. R., and Mason, P. "Concentration fluctuation measurements in a dispersing plume at a range of up to 1000 m," *Quarterly Journal of the Royal Meteorological Society* Vol. 117, No. 497, 1991, pp. 177-206.

6. Mylne, K. R. "Concentration fluctuation measurements in a plume dispersing in a stable surface layer," *Boundary-Layer Meteorology* Vol. 60, No. 1-2, 1992, pp. 15-48.

7. Connor, E. G., McHugh, M. K., and Crimaldi, J. P. "Quantification of airborne odor plumes using planar laser-induced fluorescence," *Experiments in Fluids* Vol. 59, No. 9, 2018, p. 137.

8. Webster, D., and Weissburg, M. "Chemosensory guidance cues in a turbulent chemical odor plume," *Limnology and Oceanography* Vol. 46, No. 5, 2001, pp. 1034-1047.

9. Celani, A., Villermaux, E., and Vergassola, M. "Odor landscapes in turbulent environments," *Physical Review X* Vol. 4, No. 4, 2014, p. 041015.

10. Sane, S. P., and Jacobson, N. P. "Induced airflow in flying insects II. Measurement of induced flow," *Journal of Experimental Biology* Vol. 209, No. Pt 1, 2006, pp. 43-56.

11. Loudon, C., and Koehl, M. "Sniffing by a silkworm moth: wing fanning enhances air penetration through and pheromone interception by antennae," *Journal of experimental Biology* Vol. 203, No. 19, 2000, pp. 2977-2990.

12. Li, C. "Effects of wing pitch kinematics on both aerodynamic and olfactory functions in an upwind surge," *Proceedings of the Institution of Mechanical Engineers, Part C: Journal of Mechanical Engineering Science* Vol. 235, No. 2, 2021, pp. 296-307.

13. Lei, M., and Li, C. "Numerical investigation of the passive pitching mechanism in odor-tracking flights," *AIAA paper 2020-3016*, 2020.

14. Li, C., Dong, H., and Zhao, K. "A balance between aerodynamic and olfactory performance during flight in Drosophila," *Nature Communications* Vol. 9, No. 1, 2018, p. 3215.

15. Li, C., Dong, H., and Zhao, K. "Dual functions of insect wings in an odor-guided aeronautic navigation," *Journal of fluids engineering* Vol. 142, No. 3, 2020.

16. Haverkamp, A., Yon, F., Keesey, I. W., Mißbach, C., Koenig, C., Hansson, B. S., Baldwin, I. T., Knaden, M., and Kessler, D. "Hawkmoths evaluate scenting flowers with the tip of their proboscis," *Elife* Vol. 5, 2016, p. e15039.

17. Li, C., Dong, H., and Cheng, B. "Effects of aspect ratio and angle of attack on tip vortex structures and aerodynamic performance for rotating flat plates," *AIAA 2017-3645*, 2017, p. 3645.

18. Wang, J., Li, C., Zhu, R., Liu, G., and Dong, H. "Wake structure and aerodynamic performance of passively pitching revolving plates," *AIAA paper 2019-1376*, 2019.

19. Li, C., Dong, H., and Cheng, B. "Tip vortices formation and evolution of rotating wings at low Reynolds numbers," *Physics of Fluids* Vol. 32, No. 2, 2020, p. 021905.

20. Li, C., and Dong, H. "Three-dimensional wake topology and propulsive performance of low-aspect-ratio pitching-rolling plates," *Physics of Fluids* Vol. 28, No. 7, 2016, p. 071901.

21. Xu, M., Wei, M., Li, C., and Dong, H. "Adjoint-based optimization for thrust performance of three-dimensional pitching–rolling plate," *AIAA Journal* Vol. 57, No. 9, 2019, pp. 3716-3727.

22. Li, C., Dong, H., and Liu, G. "Effects of a dynamic trailing-edge flap on the aerodynamic performance and flow structures in hovering flight," *Journal of Fluids and Structures* Vol. 58, 2015, pp. 49-65.

23. Wang, J., Li, C., Ren, Y., and Dong, H. "Effects of Surface Morphing on the Wake Structure and Performance of Flapping Plates," *AIAA 2017-3643*, 2017, p. 3643.

24. Li, C., and Dong, H. "Quantification and Analysis of Propulsive Wake Topologies in Finite Aspect-Ratio Pitching-Rolling Plates," *AIAA Paper 2016-4339*, 2016.

25. Li, C., and Dong, H. "Wing kinematics measurement and aerodynamics of a dragonfly in turning flight," *Bioinspiration & Biomimetics* Vol. 12, No. 2, 2017, p. 026001.

26. Li, C., Wang, J., Liu, G., Deng, X., and Dong, H. "Passive pitching mechanism of three-dimensional flapping wings in hovering flight," *ASME-JSME-KSME 2019 8th Joint Fluids Engineering Conference*. American Society of Mechanical Engineers Digital Collection, 2019, pp. AJKFluids2019-4639, V002T02A043.

27. Lei, M., and Li, C. "The aerodynamic performance of passive wing pitch in hovering flight," *Physics of Fluids* Vol. 32, No. 5, 2020, p. 051902.

28. Yan, Y., and Zu, Y. "Numerical simulation of heat transfer and fluid flow past a rotating isothermal cylinder–a LBM approach," *International Journal of Heat and Mass Transfer* Vol. 51, No. 9-10, 2008, pp. 2519-2536.

29. Richter, A., and Nikrityuk, P. A. "Drag forces and heat transfer coefficients for spherical, cuboidal and ellipsoidal particles in cross flow at sub-critical Reynolds numbers," *International Journal of Heat and Mass Transfer* Vol. 55, No. 4, 2012, pp. 1343-1354.